

A Dataset-free Self-supervised Disentangled Learning Method for Adaptive Infrared and Visible Images Super-resolution Fusion

Yuanjie Gu, Zhibo Xiao, Hailun Wang, Cheng Liu, and Shouyu Wang

Abstract—This study proposes a novel general dataset-free self-supervised learning framework based-on physical model named self-supervised disentangled learning (SDL), and proposes a novel method named Deep Retinex fusion (DRF) which applies SDL framework with generative networks and Retinex theory in infrared and visible images super-resolution fusion. Meanwhile, a generative dual-path fusion network ZipperNet and adaptive fusion loss function Retinex loss are designed for effectively high-quality fusion. The core idea of DRF (based-on SDL) consists of two parts: one is generating components which are disentangled from physical model using generative networks; the other is loss functions which are designed based-on physical relation, and generated components are combined by loss functions in training phase. Furthermore, in order to verify the effectiveness of our proposed DRF, qualitative and quantitative comparisons compared with six state-of-the-art methods are performed on three different infrared and visible datasets. Our code will be open source available soon at <https://github.com/GuYuanjie/Deep-Retinex-fusion>.

Index Terms—Infrared and visible images fusion, self-supervised learning, dataset-free learning, disentangled learning.



1 INTRODUCTION

Infrared and visible images fusion is a challenging task in image signal processing field. The infrared sensor is sensitive to wavelengths between 8-14 μm [1], infrared images are obtained by measuring the amount of heat radiated from objects and can highlight thermal radiation objects even under poor lighting conditions or in the case of severely occluded. Meanwhile, the visible sensor is sensitive to wavelengths between 300-530 nm [2], it captures reflected light and has abundant texture details. Therefore, infrared imaging has extensive applications, such as non-destructive testing, unmanned depth of field estimation, hot spots in equipment or the location of heat loss in buildings, in the medical field to measure local differences in body surface temperature, in the rapid detection of heat leaks in nuclear power plant cooling systems, and safety protection. However, visible imaging has more extensive applications almost everywhere. Furthermore, compare to visible images, infrared images are low resolution, low contrast, low signal-to-noise ratio and visual blur. Hence an infrared and visible images super-resolution fusion result can effectively improve the ceiling of those applications.

The past 5 years have seen a great progress in deep learning study. Meanwhile, an increasing number of studies in infrared and visible images fusion based-on deep learning are obtained good performance. Due to the limitation of optical system and physical principle, we almost impossible obtain real fused image directly, it also means that the essential element: real label in supervised deep learning can not obtained, therefore, most of these works are self-supervised and can be divided into almost two categories: with training phase [3], [4], [5] and without training phase [6], [7]. For methods with training phase, they can be second divided into two categories: CNN based [3], [5], [8] and GAN based [4], [9], [10] according to type of networks. The detailed exposition of these methods will be discussed later in Sec. II-A. However, these methods have some drawbacks: some methods are not end-to-end framework [6], [11],

Manuscript received xxxx xx, xxxx; revised xxxx xx, xxxx, accepted xxxx xx, xxxx. Date of publication xxxx xx, xxxx; date of current version xxxx xx, xxxx. This work was supported by xxxxxxxx The associate editor coordinating the review of this manuscript and approving it for publication was Prof. xxx xx. (Corresponding author: Shouyu Wang.)

Yuanjie Gu, Zhibo Xiao, Hailun Wang, Cheng Liu, and Shouyu Wang are with the Computational Optics Laboratory, School of Science, Jiangnan University, Wuxi, Jiangsu 214122, China (yuanjie_gu; zhibo_xiao; hailun_wang}@stu.jiangnan.edu.cn, chengliu@siom.ac.cn, shouyu@jiangnan.edu.cn).

they use CNN to extract deep feature, while conventional fusion methods are used to fuse, therefore, the design of fused rules are more and more complex; some methods are end-to-end framework, while facing the lack of real fused ground truth, these methods solve it only relying on respective design of loss function or network, it is comprehensive; and the purpose of some GAN methods is to force the generator generating the fused image which is similar

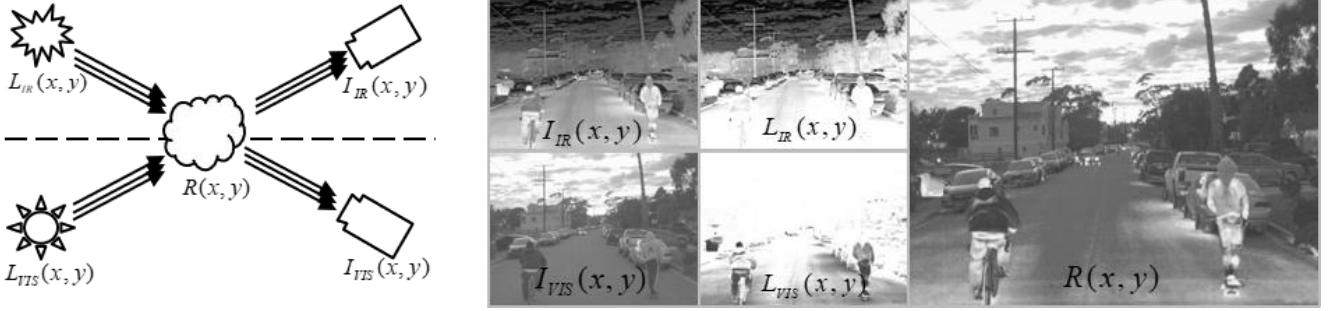


Fig. 1. Retinex theory and samples of DRF

to infrared and visible source image at the same time, while relation of infrared and visible image in this process is not one-to-one and even not linear, it is inappropriate. For methods without training phase, they often use pre-trained models which can be used to extract multilevel deep features and then the fused image is reconstructed. However, these pre-trained models are trained for other tasks, it is not fit to the infrared and visible images fusion.

In order to solve these drawbacks in infrared and visible images fusion, we propose a self-supervised disentangled learning method based-on Retinex [12] theory named Deep Retinex Fusion (DRF). As can be seen in Fig. 1, Retinex theory describe that the real world is lightless, and the lightness we perceive is the result of the interaction of light (radiation) with matter, and the process can be formulized as (1).

$$I(x, y) = R(x, y) \cdot L(x, y) \quad (1)$$

where I is the image which captured by sensor, R is the real world object, L is the light (radiation) source. Retinex is different from conventional linear and nonlinear methods, which can only enhance one type of image features, it is based on lightness consistency. It can balance dynamic range compression, edge enhancement and lightness constancy, thus enabling adaptive enhancement of various types of images. Inspired by the above theory, we implement a novel deep learning version of Retinex named DRF using generative networks and design a novel loss function named Retinex loss based-on Retinex theory. The major contributions of our DRF can be summarized as following aspects.

- We propose a novel general dataset-free self-supervised learning framework based-on physical model named self-supervised disentangled learning. The core idea of it consists of two parts: one is generating components which are disentangled from physical model using generative networks; the other is loss functions which are designed based-on physical relation, then generated components are combined by loss functions.
- We design a novel a dual path feature switching and skipping network named ZipperNet. It is a generative features fusion network based-on autoencoder. ZipperNet can implement good deep features fusion with delay features switching and good generative quality with skipping connections. Meanwhile, we design a novel Retinex loss which can adaptive balance dynamic range compression, edge enhancement and lightness constancy.
- We propose DRF which apply our ideas into Retinex theory and then implement infrared and visible images blind super-resolution fusion with it. DRF can implement one stage infrared and visible images blind super-resolution fusion rather than joint implement two respective stages. Furthermore, DRF is trained by only two source inputs and achieve state-of-the-art performance without any external datasets.

The rest of this paper is organized as follows. Section II reviews some related works and describes the idea of self-supervised disentangled learning. Section III introduces the design of DRF, the architecture of networks and the design of loss functions. In Section IV, our proposed DRF are compared with six state-of-the-art methods on several public datasets by qualitative and quantitative experiments. In Section V, we discuss the effectiveness of our designed loss functions. Finally, we conclude our study in Section VI.

2 RELATED WORKS

In this section, we review the existing generated learning works and introduce the disentangled generated learning. Furthermore, we also review the existing methods of infrared and visible image fusion.

2.1 Deep Learning-Based Fusion Methods

The past five years have seen a significant development in the study of image fusion using deep learning especially for infrared and visible image fusion. In [3] (2016), Liu et al. applied convolutional neural network (CNN) to joint generated activity level measurement and fusion rule for image fusion, the CNN trained by image patches and handcrafted blurred patches. In [13] (2018), Li et al. applied auto-coder architecture and exploited dense block into encoder part to improve the performance of infrared and visible image fusion. In the same year, [4] was the first study in infrared and visible image fusion with generative adversarial network (GAN) put forward by Ma et al., it can generate clean and clear fused images by sharpening infrared images with abundant texture details and clear highlighted targets. In [5], Zhang et al. proposed a general image fusion framework using CNN. IFCNN (2020) exploit two convolutional layers to extract deep features from input images and fused them by an appropriate fusion rule, in the end, fused image is re-

constructed by reconstructing these features. In [9] (2020), Ma et al. proposed a dual-discriminator conditional GAN for multi-resolution image fusion, the generator of DDcGAN generates fused image based on a content loss to fool the two discriminators, and the two discriminators aim to distinguish the differences between the fused image and inputs, respectively. In [14] (2020), Xu et al. proposed a novel unified unsupervised image fusion method. U2Fusion estimates the importance of source inputs and proposed adaptive information preservation degrees, therefore, this work can solve different fusion problems with the same parameters and achieve good performance. Similar to Unet [15] and Unet++ [16], in fact, NestFuse [17] (2020) likes an upgrade version of DenseFuse, it designed a nest connection-based network to extract multiscale deep features, fused them in the same scale and reconstructed fused image finally. In 2021, Li et al. also proposed a residual fusion network named RFN-Fuse [18] based-on NestFuse. Besides, RFN-Fuse also proposed a novel detail-preserving loss function and a feature enhancing loss function to improve performance.

2.2 Generative Non-data-driven Learning

Since 2018, DIP [19] first proposed that the generator network structure is sufficient to capture low-level image statistics prior to implement the inverse problems such as super-resolution, denoising and inpainting without any training data. This work provides a new point of view with implementing inverse problems, e.g. super-resolution is implemented using only self-similarity of low-resolution images and generator network. Based on DIP, Double-DIP [20] (2019) proposed that unsupervised layer decomposition tasks of a single image such as segmentation, watermark-removal and transparency separation can be implemented by coupled DIP networks. Furthermore, [21] (2020) proposed an unsupervised method to generate 3D deformable object only using raw single-view images. The core idea of it is to disentangle each input image into depth, albedo, viewpoint and illumination, and generates them by end-to-end learning. Significantly, both DIP, Double-DIP and [best-paper] are implemented based-on auto-coder (encoder-decoder) architecture. This proves that the auto-coder architectures do a good job in generative task.

However, inspired by above works, we proposed a universal generative non-data-driven unsupervised learning method named generative disentangled learning (GDL). The core idea of GDL is to disentangle the input(s) into components which are the essential parts for specific physical model (for the task to be solved) and generate them by auto-coder networks. Moreover, in order to implement non-data-driven unsupervised learning, the loss functions are designed based-on the specific physical model. Therefore, these loss functions can combine the components into a closed loop. This process is a deep mapping by using networks for a specific physical model and achieves a good performance by exploiting the self-similarity of source input(s), low-level statistics prior of source input(s) and the handcrafted prior of networks.

3 METHOD

In this section, based on Retinex theory we provide the problem formulation, the design of networks architecture and the design of loss functions for infrared and visible images super-resolution fusion.

3.1 Disentangled Deep Retinex

Based on Lightness and Retinex theory, the real world is colorless, and the color we perceive is the result of the interaction between light and matter. The basic theory of Retinex is that the color of the object is determined by the ability of the object to reflect long wave (red), medium wave (green) and short wave (blue) light, rather than by the absolute value of reflected light intensity. The color of the object is not affected by the illumination non-uniformity and has consistency. Retinex is different from traditional linear and nonlinear methods, which can only enhance one type of image features, it is based on color consistency. It can balance dynamic range compression, edge enhancement and color constancy, thus enabling adaptive enhancement of various types of images. These properties can significantly improve the inconsistency of IR and VIS fusion. For single scale Retinex, as (1) shown, we can also comprehend (1) in the other perspective that the recorded image $I(x,y)$ can be disentangled into reflection image $R(x,y)$ and lighting image $L(x,y)$.

Based on above theory, the super-resolution fused image of IR and VIS can be seen as the reflection image $R(x,y)$, and we formulate the infrared and visible images fusion model as a conditional generated model by ZipperNet, LightingNet and AdjustingNet. As the Fig. 2 shown, ZipperNet is designed for generating the super-resolution fusion image (reflection image $R(x,y)$); LightingNet is designed for generating the transform maps (lighting image $L(x,y)$); Meanwhile, due to the limitation of infrared imaging, it often obtains low-resolution results, so it is significant to improve the resolution of them. Therefore, the self-similarity of image and the deep prior of network are exploited to improve the resolution of the fused image by embedding a down-sampling layer behind the ZipperNet. Additionally, in order to adjust the overall lightness of the generated super-resolution fusion image, the AdjustingNet is designed to regression two parameters α_1 and α_2 . These generated networks are the “CPUs” of the Deep Retinex Fusion model. Furthermore, the Retinex loss is designed to construct the relation between the input images $I(x,y)$, the super-resolution fusion image $R(x,y)$, the transform maps $L(x,y)$ and the adjusting parameters α_1 and α_2 , and it is the “bus” of the Deep Retinex Fusion model.

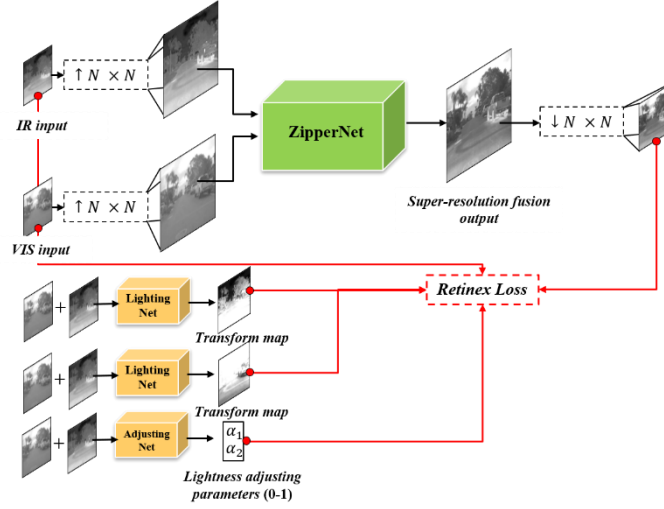


Fig. 2. DRF framework

3.2 Networks Architecture

Section 3.1 describes the framework of our Deep Retinex Fusion, there are mainly two types “CUPs” in it : ZipperNet which is a dual path feature switching and skipping network is employed to generate the super-resolution fusion image; LightingNets which are the single path feature skipping networks is employed to generate the transform maps of IR and VIS; and AdjustingNet is the same single path feature skipping network of LightingNets, but only the center-pose(s) (one or two) pixel(s) is/are used as the overall lightness adjusting parameter(s). Essentially, all of these networks are encoder-decoder architecture, this architecture perform significant well in generated tasks especially image-to-image translation [19], [20], [21], [22].

3.2.1 ZipperNet

The architecture of ZipperNet is illustrated in Fig. 3 (a). The ZipperNet is a dual path feature switching and skipping network, it has ability to handle various inputs and fused their deep features well. The inputs are the interpolations of N -scale low-resolution IR and VIS images, and must be the same shape. The backbone of ZipperNet are composed of 10 encoder- and 5 decoder-blocks, and they are symmetric about the mirror line. Each encoder-block is composed of two 1-stride 3×3 convolution layer with reflection padding to extract feature, batch normalization layer to prevent gradient explosions and vanishes, leaky-ReLU activating layer, a 1-stride 3×3 convolution layer and a 2-stride 3×3 convolution layer to down-sample, batch normalization layer and leaky-ReLU layer, successively. These encoder blocks construct the dual path encoder, in order to fuse the deep feature better, the features in different odd-even layers are added onto the same-depth layer in the other path. Identically, Each decoder-block is composed of a $\times 2$ bilinear layer to up-sample , a batch normalization layer, two 1-stride 3×3 convolution layer with reflection padding, a batch normalization layer, a leaky-ReLU layer, two 1-stride 3×3 convolution layer with reflection padding, a batch normalization layer and leaky-ReLU layer. Furthermore, in order to fuse the features between encoder and decoder part, the skip connections which are symmetric about the mirror line are adopted to concatenate the features. In the end of the ZipperNet, a sigmoid activation function is adopted to format the value range of the output. For some details, the numbers of convolution kernels in every same depth encoder-block are 8, 16, 32,64 and 128, and 128, 64, 32, 16 and 8 in every decoder-block.

3.2.2 LightingNet & AdjustingNet

LightingNet and AdjustingNet are the same architecture in fact, the architecture of is illustrated in Fig. 3 (b), and it is a single path version encoder-decoder architecture which is very similar to ZipperNet. LightingNet and AdjustingNet are composed of 5 encoder-, 5 decoder-blocks and skipping connections which are symmetric about the mirror line alike. LightingNets are exploited to generate the transform maps. Difference to exploiting the whole output map of LightingNet, AdjustingNet only exploits the center-pose(s) pixels of the output map as the weighted parameters to adjust the lightness of the generated image. Identical to ZipperNet, the numbers of convolution kernels in every same depth encoder-block are 8, 16, 32,64 and 128, and 128, 64, 32, 16 and 8 in every decoder-block.

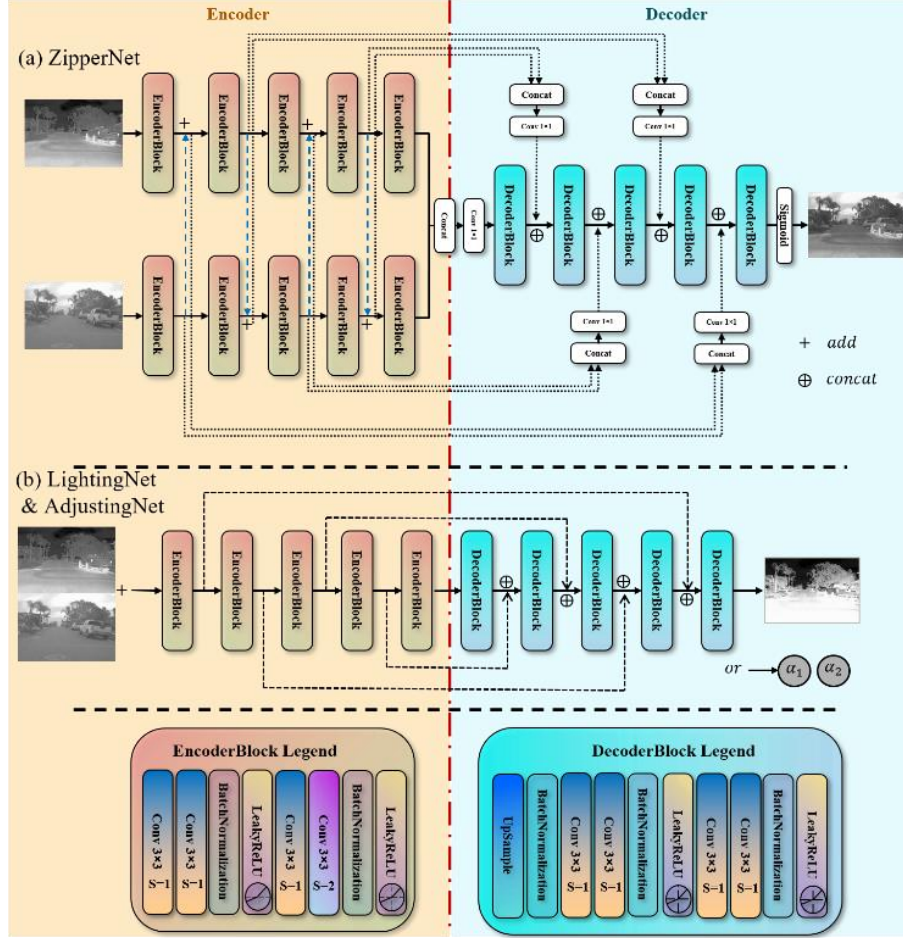


Fig. 3. Networks architecture

3.3 Loss functions

The loss functions including Retinex loss, joint gradient loss and lock losses are the “bus” which connects various components, and the Retinex loss which base on Retinex theory is the core of the Deep Retinex Fusion. The original design of Retinex loss (see (2)) depends on (1).

$$\mathcal{L}_{\text{Retinex}}^* = \frac{1}{H \cdot W} \sum_i \sum_j \left(|R_{i,j} \cdot L_{i,j}^1 - I_{i,j}^1| + |R_{i,j} \cdot L_{i,j}^2 - I_{i,j}^2| \right) \quad (2)$$

where H and W are the height and width of the image, R is the generated image of ZipperNet, L^1 and L^2 are the generated images of LightingNets, I^1 and I^2 are the input IR and VIS images, i and j are the indexes of pixels. L1 norm is adopted here which has proved having better performance than L2 norm in SR tasks in [23].

However, the random initialization generated results of R and L have high probability existing zero value, and any one zero value of them will cause instability via dot. Meanwhile, untreated maps R and L have high lightness dynamic range which is difficult to limit. Therefore, in order to resolve these limitations, we apply \log on (1) to transfer dot into add (see (3)), and reduce the lightness dynamic range of R and L , respectively.

$$\log I(x, y) = \log R(x, y) + \log L(x, y) \quad (3)$$

The optimized design of Retinex loss (see (4)) depends on (3).

$$\mathcal{L}_{\text{Retinex}} = \frac{1}{H \cdot W} \sum_i \sum_j \left\{ \left| \alpha_1 \cdot (\log |R_{i,j} + c| + \log |L_{i,j}^1 + c|) - \log |I_{i,j}^1 + c| \right| \right. \\ \left. + \left| \alpha_2 \cdot (\log |R_{i,j} + c| + \log |L_{i,j}^2 + c|) - \log |I_{i,j}^2 + c| \right| \right\} \quad (4)$$

In order to avoid zero and negative values in \log , we apply the small bias c ($=10^{-7}$) and abs before applying \log . Although the optimized Retinex loss can successful work, because of additional maps L which act on R , the overall fused image is darker than inputs. Therefore, additional α_1 and α_2 ($0 < \alpha_1, \alpha_2 < 1$) are the weighted learnable parameters which generated by AdjustingNet, they so as to improve the visual lightness perception of fused image.

In IR and VIS fusion, the more high-frequency information the better for applications. Thus, the maximum gradient map can almost represent the fused gradient map. The joint gradient loss (7) is designed to keep the network pay more attention to high-frequency information. ∇ is the Laplacian gradient.

$$\mathcal{L}_{\text{joint}}^{\text{grad}} = \frac{1}{H \cdot W} \sum_i \sum_j |\nabla R_{i,j} - \max(\nabla I_{i,j}^1, \nabla I_{i,j}^2)| \quad (5)$$

Furthermore, there is no limitation on transform maps L and lightness weighted parameters α_1 and α_2 during the iterations. Thus, the L and α lock losses (see (5) and (6)) are designed to limit the value range of L , α_1 and α_2 .

$$\mathcal{L}_{\text{lock}}^L = \frac{1}{H \cdot W} \sum_i \sum_j (|L_{i,j}^1 - 1| + |L_{i,j}^2 - 1|) \quad (6)$$

$$\mathcal{L}_{\text{lock}}^\alpha = |\alpha_1 - 0.5| + |\alpha_2 - 0.5| \quad (7)$$

Based on the Retinex loss, another lightness lock loss (see (7)) is designed to keep the lightness degree of the generated fused image approaching to the inputs.

$$\mathcal{L}_{\text{lock}}^{\text{mean}} = \frac{1}{H \cdot W} \sum_i \sum_j (\bar{R} - \frac{\bar{I}^1 + \bar{I}^2}{2}) \quad (8)$$

where \bar{x} is the mean pixel value of x . In general, the total loss is shown as (8), and the values of λ_1 , λ_2 , λ_3 , λ_4 and λ_5 are often 1, 0.2 ± 0.1 , 0.25, 0.25 and 1 in our experience.

$$\mathcal{L}_{\text{total}} = \lambda_1 \cdot \mathcal{L}_{\text{Retinex}} + \lambda_2 \cdot \mathcal{L}_{\text{joint}}^{\text{grad}} + \lambda_3 \cdot \mathcal{L}_{\text{lock}}^L + \lambda_4 \cdot \mathcal{L}_{\text{lock}}^\alpha + \lambda_5 \cdot \mathcal{L}_{\text{lock}}^{\text{mean}} \quad (9)$$

4 EXPERIMENTAL RESULTS

4.1 Qualitative Experiments

In order to verify the effectiveness of proposed DRF, we compare it with several existing state-of-art models including DDcGAN [9], DenseFuse [13], IFCNN [5], RFN-Nest [18], NestFuse [17] and U2Fusion [14] on $\times 2$ scale of blind super-resolution fusion on FLIR¹, TNO² and VIFB³ datasets by qualitative comparisons. Additionally, we also compare the $\times 4$ scale of blind super-resolution fusion on FLIR. Due to the competitors work without super-resolution and we implement super-resolution only using a simple down-sampling, therefore, we up-sample the results of these competitors using Bicubic to keep the comparisons are identical standard to ours.

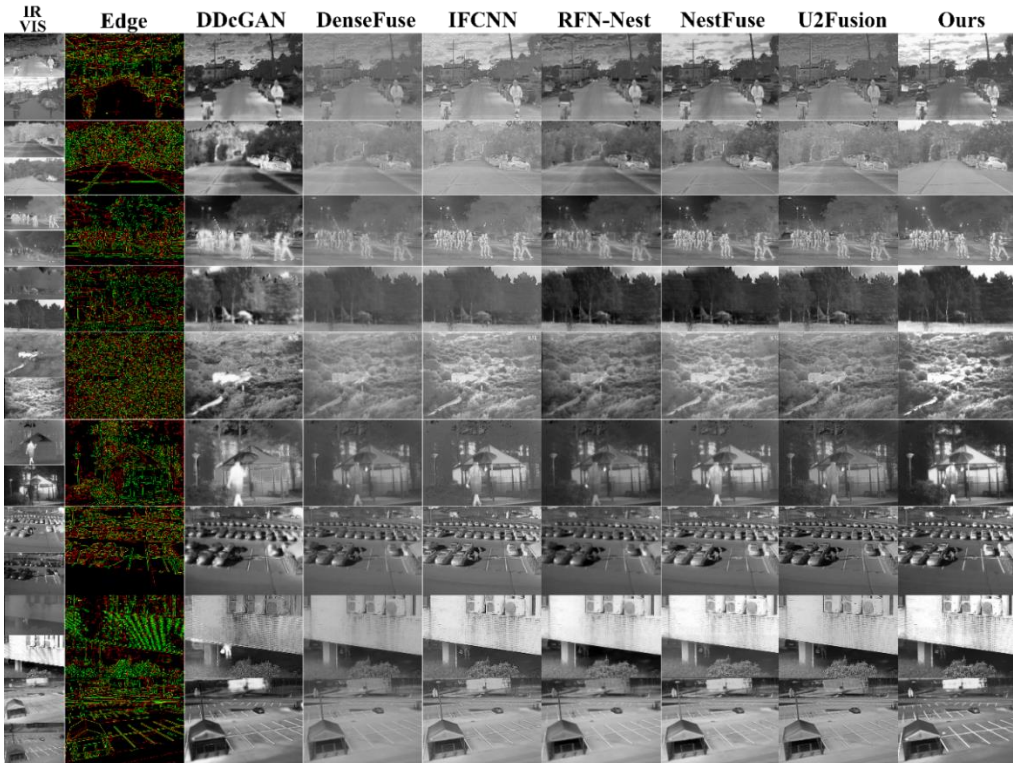


Fig. 4. $\times 2$ scale of blind super-resolution fusion on FLIR¹, TNO² and VIFB³ datasets

The $\times 2$ scale comparisons can be seen from Fig. 4, we randomly chose three results in each dataset. The $\times 4$ scale comparisons can be seen from Fig. 6, we randomly chose two daytime and two night results in FLIR. It is easy to note that the results of our DRF have the best comprehensive performance. Compared with other six methods, our advantages can be summarized as three point. First, DRF can integrate the high contrast properties of IR images into visible images perfectly and maintain the real visible information in the meantime. Second, DRF can preserve abundant visible texture details. Actually, the high temperature objects often are paid more attention in the IR images, therefore, an ideal fused image almost fuse the information of these high temperature objects to visible image rather than other nonsignificant information in IR image. DRF does a good job of this especially with the distinction between day and night scenes. Third, our results are much more resistant to noise, as Fig. 5 shown, we use [24] to blind estimate the noise level of the sample which has much noise in TNO. Compared with three methods which can process noise well, our result has the lowest noise level. In general, our results are more natural, overall and clearer.

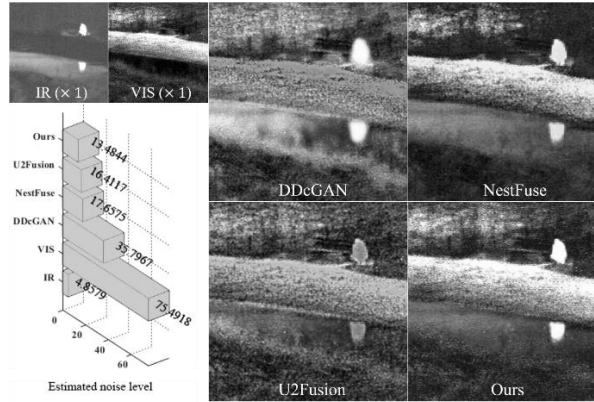
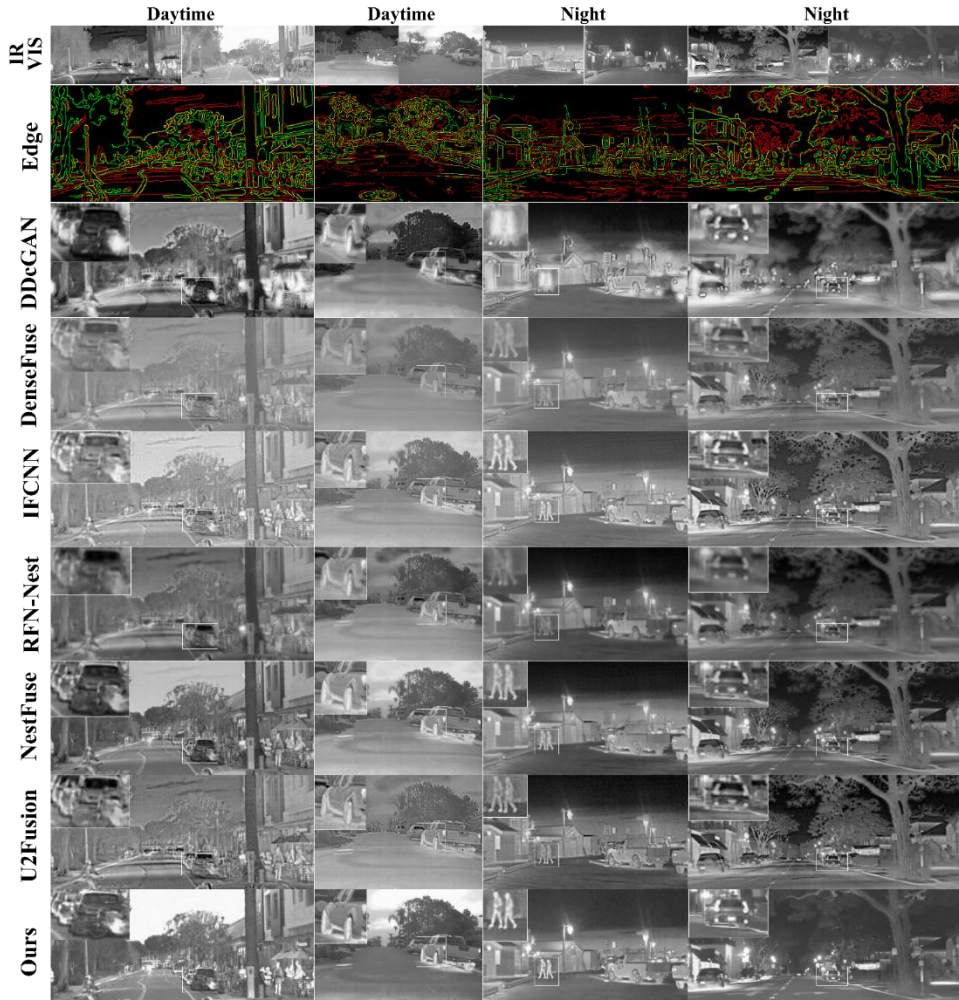


Fig. 5. Noise level comparison

Fig. 6. $\times 4$ scale of blind super-resolution fusion on FLIR

4.2 Quantitative Experiments

We further compare the quantitative experiments of our DRF with the other competitors on the $\times 2$ and $\times 4$ scale of blind super-resolution fusion on FLIR (Table 1), and additional $\times 2$ scale on TNO and VIFB datasets (Table 2). The metrics are composed of mean gradient (MG), cross entropy (CEN), edge intensity (EI) and spatial frequency (SF). MG can reflect the high frequency information content of the fused image and reflect the image quality, the higher is better. CEN can reflect the similarity of image information distribution between source images and fused image, the lower is better. EI can reflect the amplitude of edge intensity calculated by Sobel operator, the higher is better. And SF can reflect the texture details richness, the higher is better. Moreover, the proposed DRF can achieve the best metrics values in all experiments. Additionally, the four metrics performances of every image pairs in FLIR are shown in Fig. 7.

TABLE 1 COMPETITORS ON THE $\times 2$ AND $\times 4$ SCALE OF BLIND SUPER-RESOLUTION FUSION ON FLIR

	Scale	DDcGAN []	DenseFuse []	IFCNN []	RFN-Nest []	NestFuse []	U2Fusion []	Ours
Training Data	----	$\sqrt{\quad}$	$\sqrt{\quad}$	$\sqrt{\quad}$	$\sqrt{\quad}$	$\sqrt{\quad}$	$\sqrt{\quad}$	\times
MG \uparrow	$\times 2$	2.8224	2.0512	3.6517	1.9033	3.0943	3.7888	4.0045
	$\times 4$	1.4542	1.0667	1.8914	0.9801	1.5994	1.9575	2.2802
CEN \downarrow	$\times 2$	1.0674	1.0572	1.1840	1.3543	1.1178	1.1254	0.7810
	$\times 4$	1.0682	1.1348	1.2379	1.3555	1.1736	1.1276	0.7457
EI \uparrow	$\times 2$	29.6982	21.1764	37.6496	20.3695	32.1763	38.4379	38.9259
	$\times 4$	15.8393	11.4791	20.5459	10.6633	17.3856	21.3315	23.3445
SF \uparrow	$\times 2$	6.2729	4.3099	7.6609	3.9975	6.9372	7.7557	9.1759
	$\times 4$	3.2317	2.2560	3.9545	2.0771	3.5764	3.9926	5.1841

TABLE 2 $\times 2$ SCALE ON TNO AND VIFB DATASETS

	Dataset	DDcGAN []	DenseFuse []	IFCNN []	RFN-Nest []	NestFuse []	U2Fusion []	Ours
MG \uparrow	TNO []	3.5773	1.8624	3.4286	1.6621	2.6127	3.2500	4.1126
	VIFB []	3.6503	2.0003	3.6443	2.0109	2.6237	3.2992	4.1345
CEN \downarrow	TNO []	1.3941	1.3038	1.5360	1.5506	1.5001	1.4970	1.0108
	VIFB []	6.9814	4.6489	5.2389	6.5581	7.2613	6.6250	3.6985
EI \uparrow	TNO []	35.0284	18.2814	33.8043	17.5379	26.0180	33.1625	35.4144
	VIFB []	37.5498	20.5047	37.2774	21.5663	26.9138	34.5566	39.6117
SF \uparrow	TNO []	6.5438	3.6571	6.6726	3.2651	5.3974	6.1693	8.2946
	VIFB []	8.5957	5.0724	9.2192	4.9092	7.1645	7.9476	11.3476

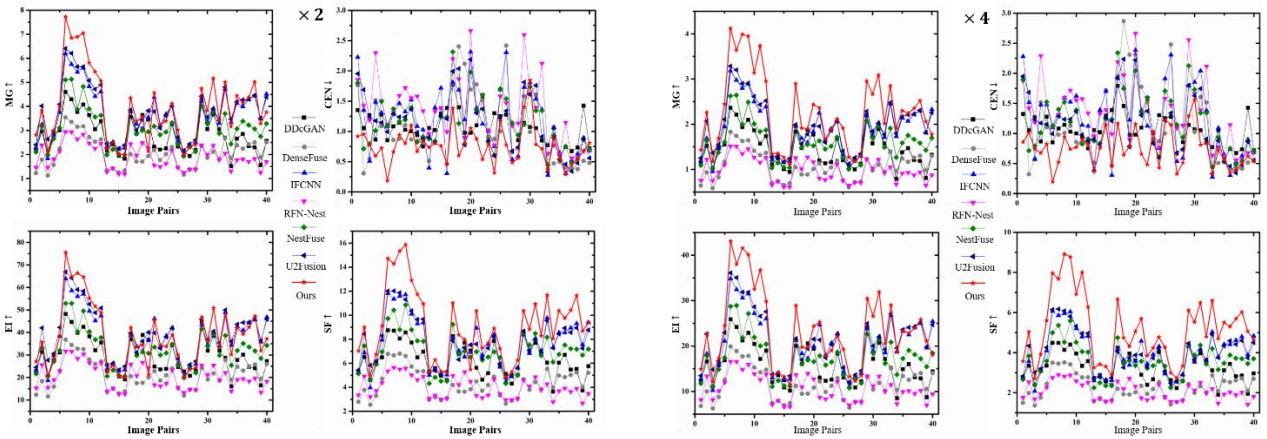


Fig. 7. $\times 2$ and $\times 4$ scale Comparisons on the FLIR

4.3 Some Implementation Details

Different from most data-drive methods, we implement our DRF with only two fixed IR and VIS inputs in every epoch rather than training dataset. Therefore, the DRF is designed for single scene fusion (like conventional iterative methods) not general scenes. In addition to this, most datasets images are gray mode both in IR and VIS, and the information and details in them are more important than color, therefore, in order to unify the process, we transfer all of inputs into

gray mode in preprocessing. The networks are training with a learning rate of 1×10^{-3} , and iterate for 10000 epochs. All of our experiments are implemented on RTX 3060 GPU.

5 DISCUSSION

In order to verify the effect of our proposed loss functions, we provide visual ablation experimental results where DRF is trained with different loss functions. As shown in Fig. 8, we discuss the effectiveness of loss functions which described in Section 3. It is easy to note that the learnable adjusting parameters α_1 and α_2 can effectively equalize the histogram (see Fig. 8 (a) and (b)); the joint gradient loss which described in (5) can retain more significant high-frequency details (see Fig. 8 (a) and (c)); the lock loss functions which described in (6) (7) and (8) can initialize and limit the learnable adjusting parameters, reflection maps and lightness level (see Fig. 8 (a) and (d)); finally, we test the Retinex loss in dot mode which described in (2), while the Retinex loss in log mode described in (4) can effectively adaptive balance the lightness (see Fig. 8 (a) and (e)). Additionally, as shown in Fig. 9, with the limitation of lock losses (7) and (8), the learnable adjusting parameters α_1 and α_2 can adaptive converge to 0-1 according to the lightness level of source inputs.



Fig. 8. Visual ablation experimental results

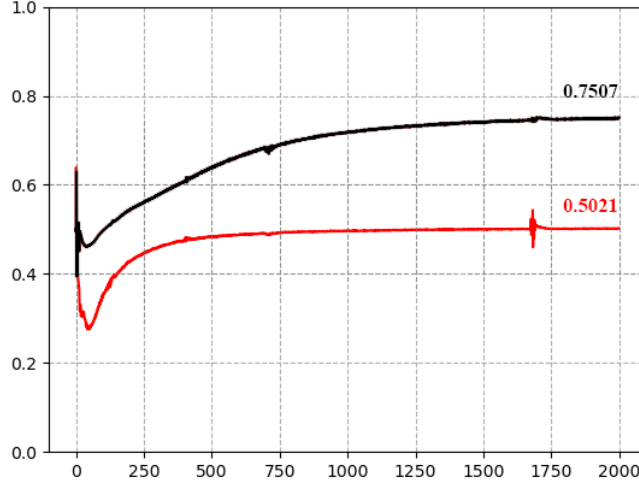


Fig. 9. The convergence analysis of learnable adjusting parameters α_1 and α_2 , red one is α_1 and black one is α_2 .

6 CONCLUSION

This study proposes a novel general dataset-free self-supervised learning framework based-on physical model named self-supervised disentangled learning (SDL), and proposes a novel method named Deep Retinex fusion (DRF) which

applies SDL framework with generative networks and Retinex theory in infrared and visible images super-resolution fusion. Meanwhile, a generative dual-path fusion network ZipperNet and adaptive fusion loss function Retinex loss are designed for effectively high-quality fusion. The core idea of DRF (based-on SDL) consists of two parts: one is generating components which are disentangled from physical model using generative networks; the other is loss functions which are designed based-on physical relation, and generated components are combined by loss functions in training phase. Furthermore, in order to verify the effectiveness of our proposed DRF, qualitative and quantitative comparisons compared with six state-of-the-art methods are performed on three different infrared and visible datasets.

REFERENCES

- [1] N. Yamamoto, T. Saito, S. Ogawa, and I. Ishimaru, "Middle infrared (wavelength range: 8 μ m-14 μ m) 2-dimensional spectroscopy (total weight with electrical controller: 1.7 kg, total cost: less than 10,000 USD) so-called hyperspectral camera for unmanned air vehicles like drones," *Algorithms Technol. Multispectral, Hyperspectral, Ultraspectral Imag.* XXII, vol. 9840, p. 984028, 2016, doi: 10.1117/12.2223358.
- [2] J. Tian et al., "Carbon quantum dots/hydrogenated TiO₂ nanobelt heterostructures and their broad spectrum photocatalytic properties under UV, visible, and near-infrared irradiation," *Nano Energy*, vol. 11, pp. 419–427, 2015, doi: 10.1016/j.nanoen.2014.10.025.
- [3] Y. Liu, X. Chen, H. Peng, and Z. Wang, "Multi-focus image fusion with a deep convolutional neural network," *Inf. Fusion*, vol. 36, pp. 191–207, 2017, doi: 10.1016/j.inffus.2016.12.001.
- [4] J. Ma, W. Yu, P. Liang, C. Li, and J. Jiang, "FusionGAN: A generative adversarial network for infrared and visible image fusion," *Inf. Fusion*, vol. 48, no. June 2018, pp. 11–26, 2019, doi: 10.1016/j.inffus.2018.09.004.
- [5] Y. Zhang, Y. Liu, P. Sun, H. Yan, X. Zhao, and L. Zhang, "IFCNN: A general image fusion framework based on convolutional neural network," *Inf. Fusion*, vol. 54, no. August 2018, pp. 99–118, 2020, doi: 10.1016/j.inffus.2019.07.011.
- [6] D. Xu, Y. Wang, X. Zhang, N. Zhang, and S. Yu, "Infrared and Visible Image Fusion Using a Deep Unsupervised Framework with Perceptual Loss," *IEEE Access*, vol. 8, pp. 206445–206458, 2020, doi: 10.1109/ACCESS.2020.3037770.
- [7] H. Li, X. jun Wu, and T. S. Durrani, "Infrared and visible image fusion with ResNet and zero-phase component analysis," *Infrared Phys. Technol.*, vol. 102, no. July, p. 103039, 2019, doi: 10.1016/j.infrared.2019.103039.
- [8] Y. Long, H. Jia, Y. Zhong, Y. Jiang, and Y. Jia, "RXDNFuse: A aggregated residual dense network for infrared and visible image fusion," *Inf. Fusion*, vol. 69, no. November 2020, pp. 128–141, 2021, doi: 10.1016/j.inffus.2020.11.009.
- [9] J. Ma, H. Xu, J. Jiang, X. Mei, and X. P. Zhang, "DDcGAN: A Dual-Discriminator Conditional Generative Adversarial Network for Multi-Resolution Image Fusion," *IEEE Trans. Image Process.*, vol. 29, no. ii, pp. 4980–4995, 2020, doi: 10.1109/TIP.2020.2977573.
- [10] Y. Long, H. Jia, Y. Zhong, Y. Jiang, and Y. Jia, "RXDNFuse: A aggregated residual dense network for infrared and visible image fusion," *Inf. Fusion*, vol. 69, no. November 2020, pp. 128–141, 2021, doi: 10.1016/j.inffus.2020.11.009.
- [11] Y. Liu, X. Chen, R. K. Ward, Z. J. Wang, and S. Member, "Sparse Representation," *Comput. Vis.*, vol. 23, no. 12, pp. 1185–1185, 2021, doi: 10.1007/978-3-030-63416-2_300100.
- [12] Edwin H. Land and John J. McCann, "Lightness and Retinex Theory," *J. Opt. Soc. Am.* 61, 1-11, 1971.
- [13] H. Li and X. J. Wu, "DenseFuse: A fusion approach to infrared and visible images," *IEEE Trans. Image Process.*, vol. 28, no. 5, pp. 2614–2623, 2019, doi: 10.1109/TIP.2018.2887342.
- [14] H. Xu, J. Ma, J. Jiang, X. Guo, and H. Ling, "U2Fusion: A Unified Unsupervised Image Fusion Network," *IEEE Trans. Pattern Anal. Mach. Intell.*, vol. 8828, no. c, pp. 1–1, 2020, doi: 10.1109/tpami.2020.3012548.
- [15] N. Navab, J. Hornegger, W. M. Wells, and A. F. Frangi, "Medical Image Computing and Computer-Assisted Intervention - MICCAI 2015: 18th International Conference Munich, Germany, October 5-9, 2015 proceedings, part III," *Lect. Notes Comput. Sci. (including Subser. Lect. Notes Artif. Intell. Lect. Notes Bioinformatics)*, vol. 9351, no. Cvd, pp. 12–20, 2015, doi: 10.1007/978-3-319-24574-4.
- [16] Z. Zhou, M. M. R. Siddiquee, N. Tajbakhsh, and J. Liang, "Unet++: A nested u-net architecture for medical image segmentation," in *Deep Learning in Medical Image Analysis and Multimodal Learning for Clinical Decision Support*. Granada, Spain: Springer, 2018, pp. 3–11.
- [17] H. Li, X. J. Wu, and T. Durrani, "NestFuse: An Infrared and Visible Image Fusion Architecture Based on Nest Connection and Spatial/Channel Attention Models," *IEEE Trans. Instrum. Meas.*, vol. 69, no. 12, pp. 9645–9656, 2020, doi: 10.1109/TIM.2020.3005230.
- [18] H. Li, X. J. Wu, and J. Kittler, "RFN-Nest: An end-to-end residual fusion network for infrared and visible images," *Inf. Fusion*, vol. 73, no. February, pp. 72–86, 2021, doi: 10.1016/j.inffus.2021.02.023.
- [19] V. Lempitsky, A. Vedaldi, and D. Ulyanov, "Deep Image Prior," *Proc. IEEE Comput. Soc. Conf. Comput. Vis. Pattern Recognit.*, pp. 9446–9454, 2018, doi: 10.1109/CVPR.2018.00984.
- [20] Y. Gandelsman, A. Shocher, and M. Irani, "'Double-dip': Unsupervised image decomposition via coupled deep-image-priors," *Proc. IEEE Comput. Soc. Conf. Comput. Vis. Pattern Recognit.*, vol. 2019-June, no. 788535, pp. 11018–11027, 2019, doi: 10.1109/CVPR.2019.01128.
- [21] S. Wu, C. Rupprecht, and A. Vedaldi, "Unsupervised Learning of Probably Symmetric Deformable 3D Objects from Images in the Wild," *IEEE Trans. Pattern Anal. Mach. Intell.*, 2021, doi: 10.1109/TPAMI.2021.3076536.
- [22] K. Zhang, Y. Li, W. Zuo, L. Zhang, L. Van Gool, and R. Timofte, "Plug-and-Play Image Restoration with Deep Denoiser Prior," *IEEE Trans. Pattern Anal. Mach. Intell.*, vol. 8828, no. c, pp. 1–17, 2021, doi: 10.1109/TPAMI.2021.3088914.
- [23] H. Zhao, O. Gallo, I. Frosio, and J. Kautz, "Loss Functions for Neural Networks for Image Processing," pp. 1–11, 2015, [Online]. Available: <http://arxiv.org/abs/1511.08861>.
- [24] X. Liu, M. Tanaka, and M. Okutomi, "Single-image noise level estimation for blind denoising," *IEEE Trans. Image Process.*, vol. 22, no. 12, pp. 5226–5237, 2013, doi: 10.1109/TIP.2013.2283400.